ARTICLE

In-situ precise anchoring of Pt single atoms in spinel Mn_3O_4 for highly efficient hydrogen evolution reaction

Received 00th January 20xx,
Accepted 00th January 20xx

DOI: 10.1039/x0xx00000x

Jinxin Wei,[a] Kang Xiao[a,*], Yanxiang Chen,[a] Xing-Peng Guo,[a] Bolong Huang[b,*] and Zhao-Qing Liu[a,*]

Although the synthesis of single atom catalysts (SAC) has attracted intensive attention for hydrogen evolution reaction (HER), realizing the precise control in the structure of atomic catalysts and the electronic metal-support interaction is still highly challenging. The understanding of SAC from the atomic level is particularly important for further improving electrochemical performances. Herein, we have reported the synthesis of a spinel Mn_3O_4 supported Pt SACs (Pt_{SA}-Mn_3O_4) based on the *in-situ* precise anchoring of the Pt atoms in the octahedral sites for the first time. The strong interactions between the Pt and Mn_3O_4 have significantly modulated the electronic structures with optimized d-band center and binding strength of intermediates. Under the alkaline environment, the catalyst shows an excellent HER performance with an ultra-low overpotential of 24 mV at 10 mA cm^{-2} and high mass activity of 374 mA mg^{-1}_{Pt} (50 mV), which is superior to 20 wt% Pt/C and the most reported high-performance catalysts. This work has supplied insightful information for the rational design of efficient SAC with high controllability and superior performances.

Introduction

Hydrogen (H_2) is one of the most promising clean energy resources providing high energy density for electricity conversion whilst with zero-pollutant emission.[1-4] Water splitting of electrocatalytic hydrogen evolution reaction (HER) powered by renewable electricity is considered a low-cost and sustainable strategy.[5-7] HER is an electrochemical process that occurs at the electrode/electrolyte interface to reduce H_3O^+ (acidic) or H_2O (alkaline) to H_2.[8-10] Platinum (Pt) is the most efficient material for catalytic HER, due to the appropriate adsorption/desorption energy towards the H intermediates. However, the low abundance and high cost of Pt severely restrict its industrial applications.[11-13] Therefore, it is necessary to develop high-performance HER catalyst while using a minimized Pt amount. Single-atom catalysts (SACs) take the advantage of maximizing the utilization of each metal centers while affording even higher performance than its aggregated clusters or nanoparticles.[14-20] For Pt-based catalysts, the slow alkaline HER kinetics are due to the high energy barrier that needs to be overcome for the water dissociation step.[21] Therefore, the rational design of catalyst structure and properties to modulate the concentration and type of active sites is essential for an efficient and stable HER catalytic process.[22-24]

Pt single-atom catalysts, with the optimized electronic structure of the catalyst through electronic metal-support interaction (EMSI) are excellent representatives to improve HER activity.[25-27] For instance, Pt single-atom sites (Pt/np-$Co_{0.85}Se$) on nanoporous cobalt selenide endowed electronic interactions between the Pt single atom sites and the np-$Co_{0.85}Se$ support, which favored the adsorption/desorption of hydrogen and, thus improved HER performance.[28] In addition, Pt single atoms immobilized on two-dimensional NiO/Ni heterostructure (Pt-NiO/Ni) and one-dimensional Ag nanowires were constructed as an excellent alkaline HER catalyst. In the constructed catalyst, the occupancy of Pt-5*d* orbitals near the Fermi energy level was enriched, combined with the modulated binding energy of reactants (OH* and H*) on the dual active sites composed of O vacancy-modified NiO and metallic Ni.[29] Furthermore, the materials with certain electron interaction between the Pt single atom sites and the support all showed excellent HER activity, including Pt single-atom anchored N-doped carbon spheres (Pt_1/NMHCS),[30] MXene nanosheets with surface Mo vacancies ($Mo_2TiC_2T_x$-Pt_{SA}),[16] and sodium titanate nanowires (Pt/NaTiO).[31] These results evidenced that EMSI helps the increased occupancy of the Pt d orbital in the Fermi level, which favors the reduction of intermediate species. Therefore, the rational construction of Pt single atom sites on a proper support is the key to improving HER. The coexistence of tetrahedral sites and octahedral sites in the spinel structure provides multiple locations for metal cations of different valence states, thus has attracted enormous research interest in electrocatalyst applications.[32, 33] In general, the electronic structure and HER activity of spinel-supported catalysts are affected by the site occupation of cation doping sites (tetrahedral or octahedral sites),[34] which provides a means of tuning the electronic structure of catalysts to enhance catalytic performance. Despite the reported Pt SACs showing excellent catalytic performance in alkaline HER, there are few direct insights focusing the combination of Pt single atom sites on Mn_3O_4 spinel, especially anchoring in the octahedral sites.

Herein, we report the preparation of porous manganese tetroxide nanosheets with Mn^{3+} vacancies (V_{Mn}-Mn_3O_4) by potential

[a]School of Chemistry and Chemical Engineering/Institute of Clean Energy and Materials/Guangzhou Key Laboratory for Clean Energy and Materials, Guangzhou University, Guangzhou 510006, China
[b]Department of Applied Biology and Chemical Technology, The Hong Kong Polytechnic University, Hung Hom, Kowloon, Hong Kong SAR, China
E-mail: kxiao@gzhu.edu.cn; lzqgzhu@gzhu.edu.cn; bhuang@polyu.edu.hk

†Electronic Supplementary Information (ESI) available: [Materials synthesis procedures, materials characterizations, DFT calculation methods, electrochemical measurements, and additional figures and tables.]. See DOI: 10.1039/x0xx00000x

ARTICLE

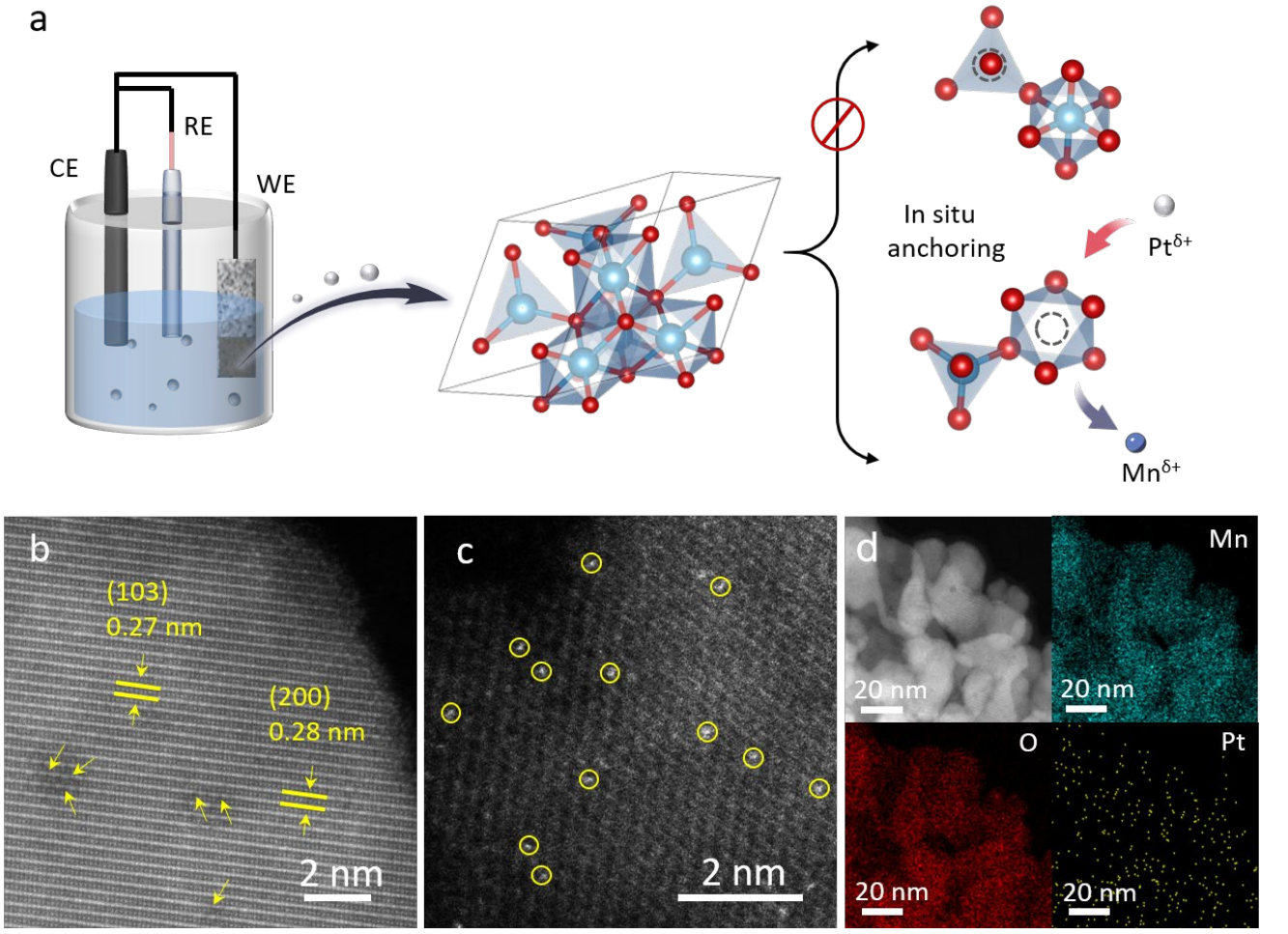

Figure 1. (a) Schematic diagram of the synthesis process. CE counter electrode, RE reference electrode, WE working electrode, The WE is Mn_3O_4. The red, blue, and grey balls refer to O, Mn, and Pt atoms, respectively. (b) HAAD-STEM images of Mn_3O_4. (c) HAADF-STEM image and (d) STEM-EDX mapping of Pt_{SA}-Mn_3O_4.

cycling method, during which the Mn^{3+} sites were partially dissolved and thus created the vacancies for the anchoring Pt single atom. Ultraviolet photoemission spectroscopy, and X-ray absorption fine structure (XAFS), verified that the Pt single atom preferably located in the octahedral site of Mn_3O_4, forming 6 O-coordinated covalent Pt-O bonds with the surrounding O atoms of Mn vacancies, stabilizing the single Pt atom. Density functional theory (DFT) calculations show the charge redistribution induced by the electron transfer from the single Pt atom sites to O atoms, increasing the energy band occupancy of the catalyst near the Fermi energy level, which facilitates the H* adsorption and the following H_2 desorption. Additionally, the single Pt atom and Mn active sites on the surface of Pt_{SA}-Mn_3O_4 exhibit better adsorption affinity for H* and OH*, respectively, since the upward shift of the *d*-band center is caused by platinum doping, which effectively improves water adsorption and dissociation. At 1 M KOH, Pt_{SA}-Mn_3O_4 (-0.919 eV) demonstrates a strong water adsorption capacity and the lowest water dissociation energy barrier (0.403 eV) compared to Mn_3O_4. Thus, the mass activity and turnover frequency (TOF) of Pt_{SA}-Mn_3O_4 were 5 and 25 times higher than those of Pt/C, respectively, at an overpotential of 50 mV. This work provides valuable insights into tuning the electronic structure in spinel oxides to obtain single-atom catalyst systems with highly efficient alkaline HER.

Results and discussion

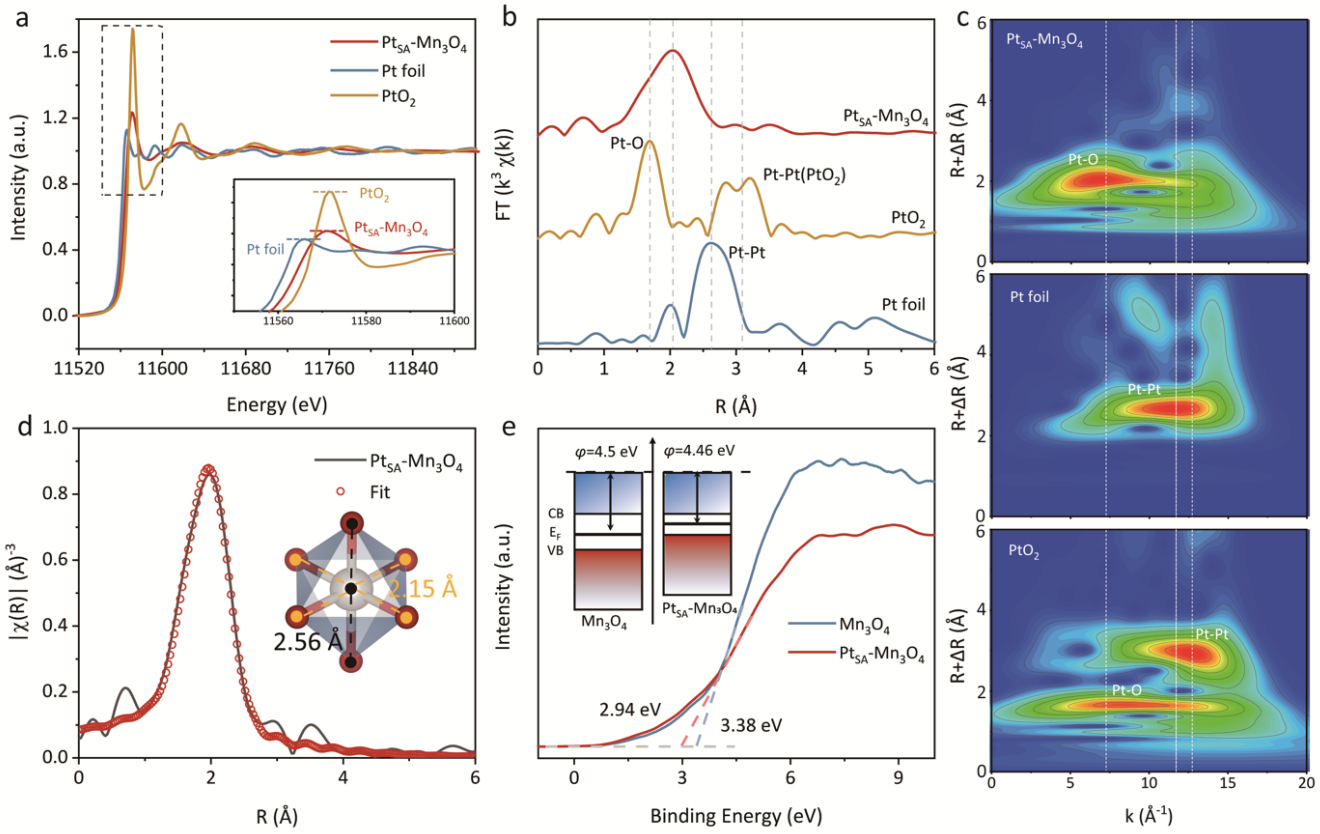

Figure 2. (a) XANES spectra, and (b) k^3-weight EXAFS spectra of Pt$_{SA}$-Mn$_3$O$_4$, Pt foil and PtO$_2$. (c) EXAFS wavelet transform plots of Pt$_{SA}$-Mn$_3$O$_4$, Pt foil and PtO$_2$. (d) FT EXAFS spectra and corresponding fitting curve of the Pt$_{SA}$-Mn$_3$O$_4$. (e) UPS valence band spectra of Mn$_3$O$_4$ and Pt$_{SA}$-Mn$_3$O$_4$.

The pure Mn_3O_4 support was prepared by electrodeposition method on Ni foam (NF) (Supplementary Figure S1). Inspired by disproportionated reaction of manganese oxides during the electrochemical charge-discharge process, vacancy generating and Pt atom anchoring were performed by cyclic voltammetry (CV) method in 0.5 M Na_2SO_4 containing 0.095 mM $H_2PtCl_6 \bullet 6H_2O$ (Figure 1a).[35, 36] During the CV cyclic process, Mn atoms gradually dissolved from the Mn_3O_4 to form Mn vacancies, which thus served as vacancy sites for subsequent deposition of Pt atoms (Figure S2).[28, 37] To optimize the content of Pt single atoms on Mn_3O_4, Different the potential cycles from 100 to 900 were applied to resulting Pt-Mn_3O_4-x samples, where x refers to potential cycles. (Figure S3 and Figure S4). The Pt loadings of Pt-Mn_3O_4-1, Pt-Mn_3O_4-3, Pt-Mn_3O_4-5, Pt-Mn_3O_4-7, and Pt-Mn_3O_4-9 were in the range of 1.58 wt.%-11.84 wt.%, as determined by inductively coupled plasma emission spectroscopy (ICP-OES Table S1). It is noteworthy that a quantitative leap in Pt loading occurs when the potential cycle exceeds 500 runs, which may be due to higher Mn vacancy generation and/or in situ nucleation of Pt growing into small clusters.[38, 39] The morphologies of Pt-Mn_3O_4-x samples were examined by scanning electron microscope (SEM) (Figure S5 and Figure S6) and transmission electron microscope (TEM). Similar to pure Mn_3O_4, the Pt-Mn_3O_4-x samples remained nanosheet structure, without showing any big Pt nanoparticles. Further, the X-ray diffraction patterns (XRD) of Pt-Mn_3O_4-x samples displayed typical characteristic peaks to Mn_3O_4, except for reduced crystallinity and a slight shift (Figure S7), no Pt peaks were observed, implying the embedding of single Pt atoms in the Mn_3O_4 lattice did not cause a phase transition.[40]

Usually, the active surface area of metallic Pt films was estimated by the electrooxidation of underpotentially deposited hydrogen, i.e., H_{upd}. Here, we used the H_{upd} as an indicator to discern the unreacted Pt single-atoms and the agglomerating Pt clusters. CV measurements were conducted in N_2-saturated 1.0 M KOH and N_2-saturated 1.0 M phosphate buffer solution (PBS).[41, 42] As shown in Figure S8, neither adsorption/desorption peaks of Pt-H nor surface

Pt-O formation/reduction peaks were observed on Pt-Mn_3O_4-1, Pt-Mn_3O_4-3, and Pt-Mn_3O_4-5. This implies that the Pt sites were atomically dispersed when the potential cycling was lower than 500 runs.[43-45] Further increase in the potential cycles led to the undesirable formation of Pt nanoparticles. This is consistent with the HER activity of Pt-Mn_3O_4-x samples, among which the Pt-Mn_3O_4-5 showed superior HER area activity (Figure S3) as well as mass activity (Figure S9). Therefore, we focused on the optimized Pt-Mn_3O_4-5 catalyst, which was denoted as Pt_{SA}-Mn_3O_4 in the following discussion.

High-angle annular dark-field scanning TEM (HAADF-STEM) in Figure 1b shows that slight Mn vacancies were observed in Mn_3O_4.[46] The bright spots appearing in Figure 1c correspond to the heavier Pt atoms, confirming the formation of single Pt atoms. Meanwhile, STEM-energy-dispersive X-ray (EDX) elemental mapping further demonstrated the uniform distribution of Mn, O, and Pt elements throughout Mn_3O_4 (Figure 1d and Figure S10). The oxidation state of platinum in Pt_{SA}-Mn_3O_4 was further analyzed by X-ray photoelectron spectroscopy (XPS). The Pt/C containing metallic Pt showed two peaks at 71.65 eV and 74.95 eV in the XPS result. Whilst in Pt 4f XPS spectrum of Pt_{SA}-Mn_3O_4, the two peaks positioned at higher binding energies, i.e., 75.23 eV and 78.43 eV, which were assigned to the oxidized Pt (II, IV) species (Figure S11). The higher binding energy shift of the Pt 4f peak of Pt_{SA}-Mn_3O_4 compared with Pt/C reveals the electron transfer from the single Pt atom in Pt_{SA}-Mn_3O_4 to the support Mn_3O_4 because of the EMSI effect between Mn_3O_4 and single-Pt-atom (Figure S12). In the Mn 2p region, the average oxidation state of the surface Mn atoms increases after the single Pt atom doping, leading to the positive shift of the Mn 2p peak (Figure S13). The location of Pt doping sites was investigated using Mn 2p XPS spectra (Figure S14). Generally, in Mn_3O_4, $Mn^{2+}(3d^5)$ atoms with a low spin state occupy the tetrahedral position, and $Mn^{3+}(3d^4)$ atoms with a high spin state occupy the octahedral position.[47-49] Comparing the fitted ratios of Mn^{2+} to Mn^{3+} for Mn_3O_4, Pt_{SA}-Mn_3O_4, and Mn_3O_4 with Mn vacancies (V_{Mn}-Mn_3O_4), the fitted ratios for the three samples were 1.08, 1.42, and 1.48, respectively, which implies that the content of Mn^{3+} decreased after cycling and a small the Mn 2p region, the average oxidation state of the surface Mn atoms increases after the single Pt atom doping, leading to the positive shift of the Mn 2p peak (Figure S13). The location of Pt doping sites was investigated using Mn 2p XPS spectra (Figure S14). Generally, in Mn_3O_4, $Mn^{2+}(3d^5)$ atoms with a low spin state occupy the tetrahedral position, and $Mn^{3+}(3d^4)$ atoms with a high spin state occupy the octahedral position.[47-49] Comparing the fitted ratios of Mn^{2+} to Mn^{3+} for Mn_3O_4, Pt_{SA}-Mn_3O_4, and Mn_3O_4 with Mn vacancies (V_{Mn}-Mn_3O_4), the fitted ratios for the three samples were 1.08, 1.42, and 1.48, respectively, which implies that the content of Mn^{3+} decreased after cycling and a small amount of Mn dissolved from Mn_3O_4 during the cycling process to form octahedral Mn vacancies. Moreover, the fitted ratios of Pt_{SA}-Mn_3O_4 and V_{Mn}-Mn_3O_4 are almost equal, and Pt_{SA}-Mn_3O_4 is slightly larger than V_{Mn}-Mn_3O_4, which may be due to the principle of charge neutralization and the formation of more Mn^{3+} vacancies in the Pt embedding process. Notably, Pt (IV) (0.63 Å) has an ionic radius similar to that of the high spin state Mn^{3+}_{hs} (0.65 Å), which facilitates Pt substitution into the Mn^{3+} site.

To further verify the relationship between the valence of Mn cations and Mn vacancies, electron spin resonance (ESR) analysis was performed. A typical Mn (II) sextet of lines was observed in the ESR spectrum of Pt_{SA}-Mn_3O_4 (Figure S15),[50-52] while similar or relatively low ESR intensities were observed in the pristine Mn_3O_4 and V_{Mn}-Mn_3O_4 samples. The ESR results further demonstrate the increase of Mn^{2+} concentration in the material, implying vacancies come from the decrease of Mn^{3+}. Figure S16a shows the characteristic Raman peaks of Mn_3O_4 with two smaller peaks located at 300-400 cm^{-1}, which belongs to the E_g vibration mode, and a sharper peak at 600-650 cm^{-1}, which belongs to the A_{1g} vibration mode.[53, 54] The A_{1g} mode corresponds to the Mn-O respiration vibration of Mn^{2+} in the tetrahedral coordination. Compared with Mn_3O_4, the A_{1g} peak of Pt_{SA}-Mn_3O_4 shifts towards a higher frequency, and the A_{1g} vibrational mode blue-shifts is related to the decreased Mn-O bond breathing frequency in the tetrahedra. The Pt doping into the octahedral sites leads to a change in the covalency of the tetrahedral Mn-O bonds connected to it, a local deformation, and a shortening of the Mn-O bonds (Figure S16b). Interestingly, with increased Pt doping, the bond length of the tetrahedral Mn-O bond is progressively shorter. Further, the electronic structure and atomic coordination environment of Pt_{SA}-Mn_3O_4 were analyzed by X-ray absorption spectroscopy (XAS).[55] According to the Pt L_3-edge X-ray absorption near edge structure (XANES) analysis (Figure 2a), the white-line intensity of the Pt_{SA}-Mn_3O_4 between Pt foil and PtO_2, indicating the positive charge state of the single-atom Pt sites in Pt_{SA}-Mn_3O_4, implying the electron transfer from Pt to O atom in the support Mn_3O_4. The intensity of the white-line peak is used as an indicator of 5*d* electronic state occupancy.[29, 30, 56] Under acidic conditions, the 5*d* orbital occupancy correlates with the binding strength of H* intermediates. But, under alkaline conditions, the 5*d* orbital occupancy correlates with the binding strength of OH* intermediates, which is significant for improving HER activity.[25] According to the WL peak intensity of Pt_{SA}-Mn_3O_4, the average oxidation state and 5*d*-electronic state occupancy of Pt is higher and reveal a strong OH* adsorption capacity, which is favorable for hydrolysis. Figure 2b shows the extended X-ray absorption fine structure (EXAFS) of Pt_{SA}-Mn_3O_4. The curve for Pt_{SA}-Mn_3O_4 exhibits a dominant peak at 2.05 Å, associated with Pt-O scattering from the first shell layer, and no Pt-Pt contributing peak, confirming the presence of single Pt atoms, in agreement with the HAADF-STEM observation. To obtain more accurate results, we performed wavelet transform (WT) analysis.[57, 58] As shown in Figure 2c, Pt_{SA}-Mn_3O_4 displays intensity maxima different from Pt foil and PtO_2, strongly confirming the Pt single atoms dispersion. Moreover, the graphs of Pt_{SA}-Mn_3O_4 and PtO_2 in the region of the radial distance of 1-2.5 Å have a high similarity, which implies the same type of bonds and elemental species coordinated to Pt atoms. Furthermore, the first-shell fitting of Pt_{SA}-Mn_3O_4 indicates that the coordination number (CN) is about 6.5 for Pt-O contributed (Figure 2d and Table S2), confirming the anchoring of Pt to the octahedral site of Mn_3O_4, where the CN about 2 for Pt-O contributed is assigned to two bonds above and below the d_z^2 axis, and Pt-O contribution with about 4 for CN is assigned to four bonds in the xy plane (Refer to the illustration in Figure 2d). It is noteworthy that the Pt-O bond in the Pt_{SA}-Mn_3O_4 sample is slightly longer than that in PtO_2, and the fitting results verify this. We also

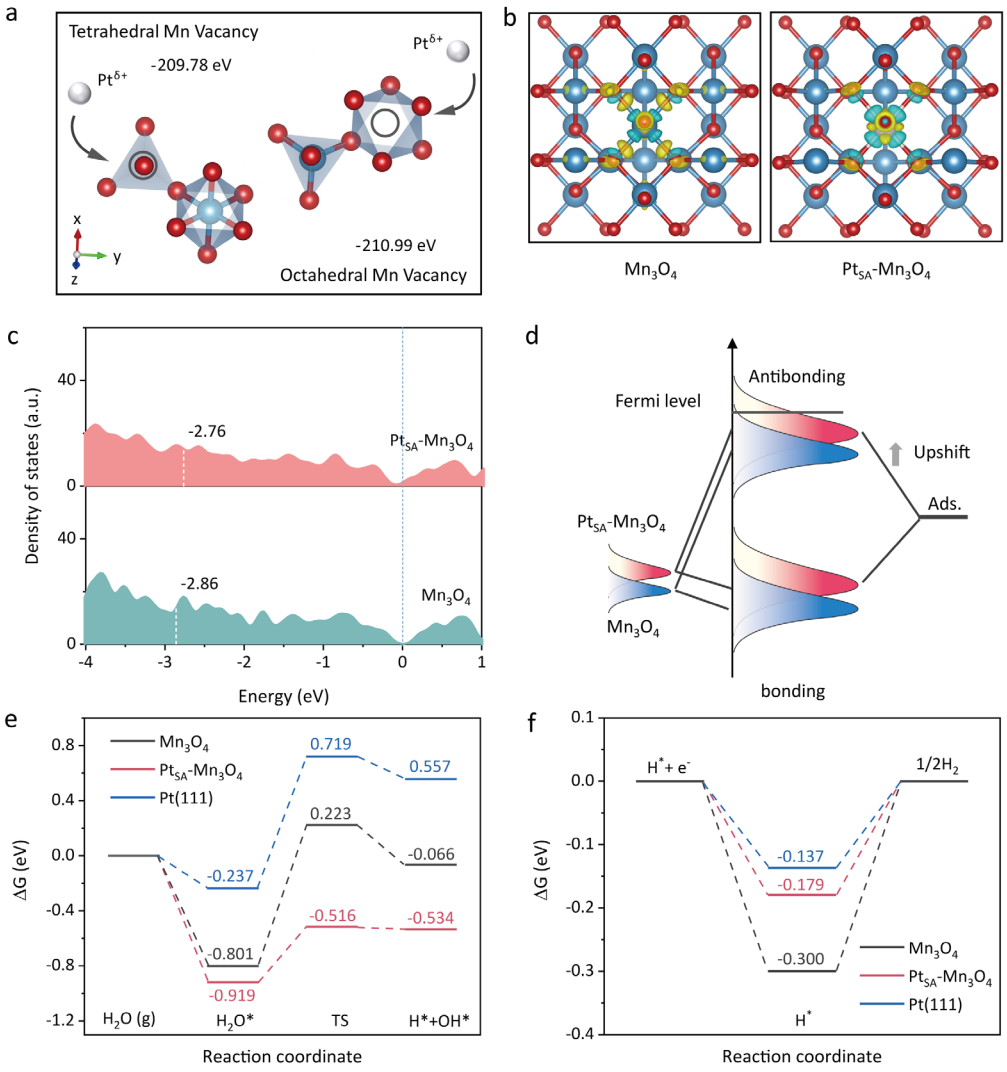

Figure 3. Density functional theory (DFT) calculations. (a) Schematic illustration of preference of Pt doping into octahedral sites of Mn_3O_4. (b) Calculated charge density distribution differences between Mn_3O_4 and Pt_{SA}-Mn_3O_4. Cyan and yellow isosurfaces represent negative and positive charges. The blue and red balls refer to Mn and O atoms. (c) Calculated PDOS of Mn_3O_4 and Pt_{SA}-Mn_3O_4. The white dashed lines represent the d-band center calculated by DFT. (d) Schematic DOS diagrams illustrating the EMSI effect on the *d*-band position of Pt_{SA}-Mn_3O_4, and bond formation between the catalyst surface and the adsorbates (Ads.). (e) Calculated Gibbs free energy for the Volmer step on the surface of Mn_3O_4, Pt (111) and Pt_{SA}-Mn_3O_4. (f) Calculated ΔG_{H^*} values of hydrogen evolution at equilibrium potential for Mn_3O_4, Pt (111) and Pt_{SA}-Mn_3O_4.

used ultraviolet photoelectron spectroscopy (UPS) to investigate the effect of Pt anchoring on the electronic structure of the catalyst (Figure 2e). The valence band maxima of Mn_3O_4 and Pt_{SA}-Mn_3O_4 are about 3.38 eV and 2.94 eV, respectively. Obviously, the valence band energy level after Pt doping is close to the Fermi level. Since the valence electrons near the Fermi level mainly originate from the *d*-band contribution, the valence band shift of Pt_{SA}-Mn_3O_4 indicates that its d-band center has also shifted.[21, 59, 60] The work function (ϕ) calculation further confirms this conclusion (refer to the inset in Figure 2e): the ϕ values are 4.5 eV and 4.46 eV for Mn_3O_4 and Pt_{SA}-Mn_3O_4, respectively, indicating that Pt embedding decreases the work function of Mn_3O_4. The lower work function means a higher *d*-band center and a weaker electron binding ability, and thus the

ARTICLE

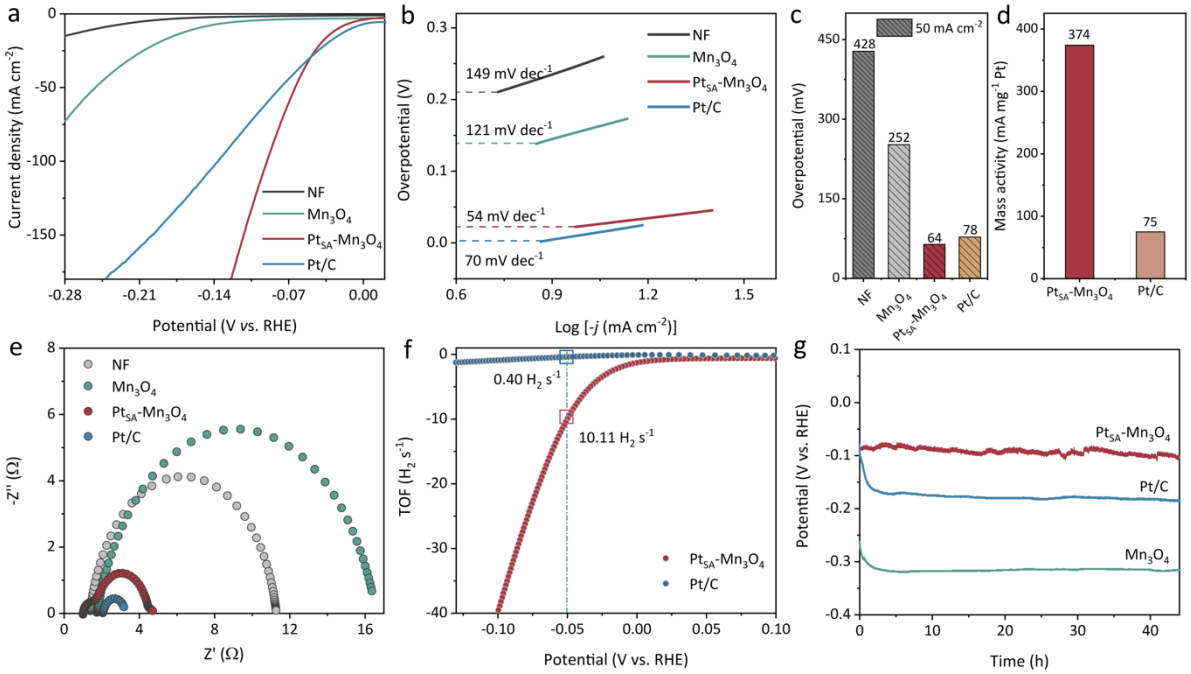

Figure 4. Electrocatalytic performance of the catalysts. (a) HER polarization curves of NF, Mn_3O_4, Pt_{SA}-Mn_3O_4 and Pt/C (with IR compensation). (b) Tafel plots obtained from the polarization curves in part a. (c) The comparison of overpotentials required to achieve 50 mA cm^{-2} for catalysts. (d) The mass activity of Pt_{SA}-Mn_3O_4 and Pt/C. (e) Nyquist plots of NF, Mn_3O_4, Pt_{SA}-Mn_3O_4 and Pt/C. (f) TOF plots of Pt_{SA}-Mn_3O_4 and Pt/C. (g) Chronopotentiometry response curves at a constant current of 10 mA cm^{-2}.

weaker electron binding facilitates the escape of electrons from the catalyst surface to participate in the catalytic reaction.

Based on the structural analysis, density functional theory calculations reveal the effect of anchoring of Pt single atom on the catalytic activity and electronic structure produced by the catalyst. According to the XRD, HAADF-STEM, and XAS results, the models of Mn_3O_4 and Pt_{SA}-Mn_3O_4 were constructed as shown in Figure S17. DFT calculations show that the total energy of a Pt atom doped into the octahedral site of the Mn_3O_4 unit cell is 1.21 eV lower than that of the doped tetrahedral site, confirming the Pt is thermodynamics favorable to locate in the octahedral site (Figure 3a). According to the charge density difference calculated in Figure 3b and Figure S18, the Pt single atom embedded in Mn_3O_4 caused a charge redistribution in the octahedral region of the Pt bond because of the different electronegativity of the Pt and O atoms (1.55 for Mn, 2.28 for Pt, 3.44 for O). The cyan region represents the depletion of charge density around the single-atom Pt, charge transfer from the Pt atom to the bonded O atom due to the strongly EMSI effect. Moreover, the calculated total and partial density of states (PDOS, Figure S19) reveal that the PDOS of Pt_{SA}-Mn_3O_4 shows a new occupied state near the Fermi level, indicating a stronger hybridization between Pt and O orbitals, and the PDOS of Pt-immobilized Mn_3O_4 shows higher occupancy near the Fermi energy level (E_F), which in summary suggests that the addition of Pt promotes electron transfer and higher electrical conductivity. Based on Nørskov's *d*-band center theory, when an adsorbed molecule approaches the catalyst surface, the orbitals of the adsorbed species interact electronically with the metal orbitals, thus leading to energy level splitting.[61, 62] The stability of the system depends on the position of the antibonding orbital generated by the energy level splitting: antibonding states above the Fermi energy level favor the adsorption of H* (acidic) or OH* (alkaline) intermediates during HER, and vice versa. When the Pt single atom sites anchor in the octahedral site, the Pt d orbital hybridizes with the p orbital of the O atom on the support, and electron transfer occurs in the Pt bonding region, which causes the *d*-band center (E_d) of Pt_{SA}-Mn_3O_4 to the upshift (Figure 3c). Will have more adsorbate antibonding states pulled above the E_F and enhance the interaction between the adsorbed molecule and Pt_{SA}-Mn_3O_4 (Figure 3d).[63] The valence band is close to the E_F energy level after Pt doping, which is consistent with the results of UPS. Based on the above analysis, we further investigated the energy barriers of the catalyst during the HER process under alkaline conditions. We found that Pt_{SA}-Mn_3O_4 exhibited the strongest adsorption capacity for H_2O (-0.919 eV,

Figure 3e) compared to Mn_3O_4 (-0.801 eV) and Pt (111) (-0.237 eV). In addition, Pt_{SA}-Mn_3O_4 exhibits an optimal water dissociation energy barrier (0.403 eV) due to the upshift of the E_d energy level, and the strong interaction of the OH* intermediate with the Pt_{SA}-Mn_3O_4 surface promote water dissociation. In the subsequent step, Figure 3f shows a hydrogen adsorption free energy (ΔG_{H^*}) value of -0.179 eV for Pt_{SA}-Mn_3O_4 at the single-atom Pt site, which is close to that of Pt (111) (-0.137 eV). These results suggest that the Mn_3O_4-supported single Pt atom can effectively enhance the *d*-band occupancy of the catalyst near the Fermi level, which will facilitate the adsorption and dissociation of H_2O and H*, and improve the catalytic activity of HER under alkaline conditions.

The HER activity of Pt_{SA}-Mn_3O_4 was evaluated in 1 M KOH electrolyte. For comparison, we also tested the HER performance for Ni form support, pure Mn_3O_4, and commercial 20 wt% Pt/C. As shown in Figure 4a, Pt_{SA}-Mn_3O_4 possesses excellent intrinsic HER activity in alkaline media, requiring very low overpotentials of 24 and 90 mV to achieve current densities of 10 and 100 mA cm^{-2}, significantly better than NF, Mn_3O_4, and Pt/C catalysts. The Tafel slope in Figure 4b shows a smaller Tafel slope of 54 mV dec^{-1} for Pt_{SA}-Mn_3O_4, much lower than Mn_3O_4 (121 mV dec^{-1}), NF (149 mV dec^{-1}) and Pt/C (70 mV dec^{-1}). And the overpotential required to reach 50 mV cm^{-2} was drastically reduced (Figure 4c). The above results showed that the Pt_{SA}-Mn_3O_4 proceeded the HER process a Volmer-Heyrovsky mechanism, that is rate-determining step is the desorption of H_2 in the Heyrovsky step (Figure S20). Furthermore, the mass activity of Pt_{SA}-Mn_3O_4 at an overpotential of 50 mV is 374 mA mg^{-1}, which is 5-times higher than that of the commercial Pt/C catalysts (75 mA mg^{-1}) (Figure 4d). These results indicate that the Mn_3O_4-constrained Pt single-atom can effectively increase the HER activity and improve Pt atom utilization efficiency under alkaline conditions, and the cost is a substantial reduction. Besides, the double-layer capacitance (C_{dl}) of Pt_{SA}-Mn_3O_4 catalyst (6.10 mF cm^{-2}) was significantly improved compared with Mn_3O_4 (4.11 mF cm^{-2}), implying that the Mn_3O_4-anchored Pt single-atom has more active sites for catalytic HER (Figure S21-S22). The HER kinetics of the catalyst in the catalytic process was further investigated using EIS (Figure 4e). The results show that Pt_{SA}-Mn_3O_4 exhibits a smaller semicircle than Mn_3O_4 and NF in the Nyquist plot, mainly due to Pt hybridization with O to promote charge transfer. Moreover, we analyzed the turnover frequency of single Pt atomic sites,[64, 65] and the TOF of Pt_{SA}-Mn_3O_4 at -50 mV vs. RHE was 10.11 s^{-1}, which is 25-times higher than that of the Pt/C catalyst (0.40 s^{-1}) (Figure 4f). The long-term stability of the Pt_{SA}-Mn_3O_4 catalyst employing the chronopotentiometry method, and Figure 4g shows that Pt_{SA}-Mn_3O_4 exhibits outstanding HER stability and can remain stable for more than 45 h at a constant current of 10 mA cm^{-2} with a smaller negligible potential increase. SEM, TEM, and EDS characterization of Pt_{SA}-Mn_3O_4 also confirmed that the morphology did not change after long-term HER stability testing, and Pt, Mn, and O elements remained uniformly distributed on the nanosheets (Figure S23-24). Notably, XRD and XPS characterization further verified that no phase change occurred in Pt_{SA}-Mn_3O_4 after a long-term operation, and no Pt^0 peak was observed, with single Pt atoms still present (Figure S25). The above results mean that Pt_{SA}-Mn_3O_4 has good stability under alkaline conditions. To the best of our knowledge, the HER performance of our Pt_{SA}-Mn_3O_4 catalyst in 1-M KOH is also superior to the most recently reported advanced noble metal-based single-atom catalysts (Table S3), confirming the superiority of Pt-embedded Mn_3O_4 catalyst.

Conclusions

In summary, we reported a simple cyclic voltammetry strategy to prepare Pt_{SA}-Mn_3O_4 material as an efficient alkaline HER catalyst. The Pt single atom sites were preferentially embedded in the Mn^{3+} octahedral sites. Due to the strong EMSI effect between Pt atoms and the spinel Mn_3O_4 support, the modulated *d*-band center of Pt_{SA}-Mn_3O_4, and thus the increased E_d energy level facilitates the adsorption of OH* intermediates on the surface of Pt_{SA}-Mn_3O_4 under alkaline conditions, which vastly promotes the dissociation of water. Compared to Pt and Mn_3O_4, Pt_{SA}-Mn_3O_4 reached the lowest hydrolysis energy barrier (0.403 eV) in the Volmer step and optimized the ΔG_{H^*} (-0.179 eV). As confirmed in the electrochemical tests, the Pt_{SA}-Mn_3O_4 showed a low overpotential of 24 mV at a current density of 10 mA cm^{-2}, as well as a high TOF value (10.11 s^{-1}) and high mass activity of 374 mA mg^{-1}_{Pt} at 50 mV, which makes it one of the most advanced noble metal-based single-atom catalysts. This work provides a valuable reference for the rational design of low-cost but efficient single-atom catalysts with site-selective atom doping.

Author Contributions

J. W., K. X., and Y. C. conducted the experiments. K.X., and Z. L. conceived the idea and designed the experiments. K.X., X. G., B. H., and Z. L. analyzed the data and interpreted the results. J. W., K.X., B. H. and Z. L. co-wrote the manuscript. The results and the manuscript are commented and discussed by all authors.

Conflicts of interest

There are no conflicts to declare.

Acknowledgements

This work was supported by the National Natural Science Foundation of China (grant nos. 21805051 and 21875048), Outstanding Youth Project of Guangdong Natural Science Foundation (no. 2020B1515020028), Yangcheng Scholars Research Project of Guangzhou (no. 201831820), and Science and Technology Research Project of Guangzhou (no.202002010007). Additional support was provided by Feringa Nobel Prize Scientist Joint Research Center.

Notes and references

1. H. B. Gray, *Nat. Chem.*, 2009, **1**, 112-112.
2. A. Turner John, *Science*, 2004, **305**, 972-974.

3. M. S. Dresselhaus and I. L. Thomas, *Nature*, 2001, **414**, 332-337.
4. D. Yu, Y. Ma, F. Hu, C.-C. Lin, L. Li, H.-Y. Chen, X. Han and S. Peng, *Adv. Energy Mater.,* 2021, **11**, 2101242.
5. T. Ouyang, Y. Ye, C.-Y. Wu, K. Xiao, Z.-Q. Liu, *Angew. Chem. Int. Ed.*, 2019, **58**, 4923–4928.
6. J. Chen, Q. Long, K. Xiao, T. Ouyang, N. Li, S. Ye, Z.-Q. Liu, *Sci. Bull.*, 2021, **66**, 1063–1072.
7. S. Anantharaj, S. R. Ede, K. Sakthikumar, K. Karthick, S. Mishra and S. Kundu, *ACS Catal.*, 2016, **6**, 8069-8097.
8. J. Wei, M. Zhou, A. Long, Y. Xue, H. Liao, C. Wei and Z. J. Xu, *Nano-Micro Lett.*, 2018, **10**, 75.
9. J. Zhu, L. Hu, P. Zhao, L. Y. S. Lee and K.-Y. Wong, *Chem. Rev.*, 2020, **120**, 851-918.
10. X. Zou and Y. Zhang, *Chem. Soc. Rev.*, 2015, **44**, 5148-5180.
11. J. N. Tiwari, S. Sultan, C. W. Myung, T. Yoon, N. Li, M. Ha, A. M. Harzandi, H. J. Park, D. Y. Kim, S. S. Chandrasekaran, W. G. Lee, V. Vij, H. Kang, T. J. Shin, H. S. Shin, G. Lee, Z. Lee and K. S. Kim, *Nat. Energy*, 2018, **3**, 773-782.
12. L. Zhang, L. Han, H. Liu, X. Liu and J. Luo, *Angew. Chem. Int. Ed.*, 2017, **56**, 13694-13698.
13. Y. Lei, Y. Wang, Y. Liu, C. Song, Q. Li, D. Wang and Y. Li, *Angew. Chem. Int. Ed.*, 2020, **59**, 20794-20812.
14. B. Qiao, A. Wang, X. Yang, L. F. Allard, Z. Jiang, Y. Cui, J. Liu, J. Li and T. Zhang, *Nat. Chem.*, 2011, **3**, 634-641.
15. A. Wang, J. Li and T. Zhang, *Nat. Rev. Chem.*, 2018, **2**, 65-81.
16. D. Zhao, Z. Chen, W. Yang, S. Liu, X. Zhang, Y. Yu, W.-C. Cheong, L. Zheng, F. Ren, G. Ying, X. Cao, D. Wang, Q. Peng, G. Wang and C. Chen, *J. Am. Chem. Soc.*, 2019, **141**, 4086-4093.
17. S. Ji, Y. Chen, X. Wang, Z. Zhang, D. Wang and Y. Li, *Chem. Rev.*, 2020, **120**, 11900-11955.
18. W. Zang, Z. Kou, S. J. Pennycook and J. Wang, *Adv. Energy Mater.*, 2020, **10**, 1903181.
19. H. Hu, J. Wang, B. Cui, X. Zheng, J. Lin, Y. Deng and X. Han, *Angew. Chem. Int. Ed.*, 2022, **61**, e202114441.
20. J. Lin, J. Ding, H. Wang, X. Yang, X. Zheng, Z. Huang, W. Song, J. Ding, X. Han and W. Hu, 2022, **34**, 2200559.
21. Z. Chen, Y. Song, J. Cai, X. Zheng, D. Han, Y. Wu, Y. Zang, S. Niu, Y. Liu, J. Zhu, X. Liu and G. Wang, *Angew. Chem. Int. Ed.*, 2018, **57**, 5076-5080.
22. S. Vajda and M. G. White, *ACS Catal.*, 2015, **5**, 7152-7176.
23. D. Zhao, Z. Zhuang, X. Cao, C. Zhang, Q. Peng, C. Chen and Y. Li, *Chem. Soc. Rev.*, 2020, **49**, 2215-2264.
24. S. Anantharaj, P. E. Karthik, B. Subramanian and S. Kundu, *ACS Catal.,* 2016, **6**, 4660-4672.
25. Y. Shi, Z.-R. Ma, Y.-Y. Xiao, Y.-C. Yin, W.-M. Huang, Z.-C. Huang, Y.-Z. Zheng, F.-Y. Mu, R. Huang, G.-Y. Shi, Y.-Y. Sun, X.-H. Xia and W. Chen, *Nat. Commun.*, 2021, **12**, 3021.
26. Y. Zhu, J. Sokolowski, X. Song, Y. He, Y. Mei and G. Wu, *Adv. Energy Mater.*, 2020, **10**, 1902844.
27. J. Yang, W. Li, D. Wang and Y. Li, *Adv. Mater.*, 2020, **32**, 2003300.
28. K. Jiang, B. Liu, M. Luo, S. Ning, M. Peng, Y. Zhao, Y.-R. Lu, T.-S. Chan, F. M. F. de Groot and Y. Tan, *Nat. Commun.*, 2019, **10**, 1743.
29. K. L. Zhou, Z. Wang, C. B. Han, X. Ke, C. Wang, Y. Jin, Q. Zhang, J. Liu, H. Wang and H. Yan, *Nat. Commun.*, 2021, **12**, 3783.
30. P. Kuang, Y. Wang, B. Zhu, F. Xia, C.-W. Tung, J. Wu, H. M. Chen and J. Yu, *Adv. Mater.*, 2021, **33**, 2008599.
31. X. Sui, L. Zhang, J. Li, K. Doyle-Davis, R. Li, Z. Wang and X. Sun, *J. Mater. Chem. A*, 2020, **8**, 16582-16589.
32. N. Sakai, K. Fukuda, R. Ma and T. Sasaki, *Chem. Mater.*, 2018, **30**, 1517-1523.
33. K. Shimokawa, T. Atsumi, M. Harada, R. E. Ward, M. Nakayama, Y. Kumagai, F. Oba, N. L. Okamoto, K. Kanamura and T. Ichitsubo, *J. Mater. Chem. A*, 2019, **7**, 12225-12235.
34. Z. Szotek, W. M. Temmerman, D. Ködderitzsch, A. Svane, L. Petit and H. Winter, *Phys. Rev. B*, 2006, **74**, 174431.
35. J.-X. Wei, M.-Z. Cao, K. Xiao, X.-P. Guo, S.-Y. Ye and Z.-Q. Liu, *Small Struct.*, 2021, **2**, 2100047.
36. K. Xiao, S.-L. Zhao, M. Cao, L. Zhang, N. Li and Z.-Q. Liu, *J. Mater. Chem. A*, 2020, **8**, 23257-23264.
37. R. Chen, C. Yang, W. Cai, H.-Y. Wang, J. Miao, L. Zhang, S. Chen and B. Liu, *ACS Energy Lett.*, 2017, **2**, 1070-1075.
38. X. Bao, Y. Gong, Y. Chen, H. Zhang, Z. Wang, S. Mao, L. Xie, Z. Jiang and Y. Wang, *J. Mater. Chem. A*, 2019, **7**, 15364-15370.
39. M. Tavakkoli, N. Holmberg, R. Kronberg, H. Jiang, J. Sainio, E. I. Kauppinen, T. Kallio and K. Laasonen, *ACS Catal.*, 2017, **7**, 3121-3130.
40. M. Sun, J. Ji, M. Hu, M. Weng, Y. Zhang, H. Yu, J. Tang, J. Zheng, Z. Jiang, F. Pan, C. Liang and Z. Lin, *ACS Catal.*, 2019, **9**, 8213-8223.
41. M. Tavakkoli, M. Nosek, J. Sainio, F. Davodi, T. Kallio, P. M. Joensuu and K. Laasonen, *ACS Catal.*, 2017, **7**, 8033-8041.
42. S. H. Ahn, Y. Liu and T. P. Moffat, *ACS Catal.*, 2015, **5**, 2124-2136.
43. D. Zhan, J. Velmurugan and M. V. Mirkin, *J. Am. Chem. Soc.*, 2009, **131**, 14756-14760.
44. S. Attard George, N. Bartlett Philip, R. B. Coleman Nicholas, M. Elliott Joanne, R. Owen John and H. Wang Jin, *Science*, 1997, **278**, 838-840.
45. R. Wang, C. Wang, W.-B. Cai and Y. Ding, *Adv. Mater.*, 2010, **22**, 1845-1848.
46. J. Yang, Y. Wang, M. J. Lagos, V. Manichev, R. Fullon, X. Song, D. Voiry, S. Chakraborty, W. Zhang, P. E. Batson, L. Feldman, T. Gustafsson and M. Chhowalla, *ACS Nano*, 2019, **13**, 9958-9964.
47. Y. Liu, Y. Ying, L. Fei, Y. Liu, Q. Hu, G. Zhang, S. Y. Pang, W. Lu, C. L. Mak, X. Luo, L. Zhou, M. Wei and H. Huang, *J. Am. Chem. Soc.*, 2019, **141**, 8136-8145.
48. A. Navrotsky and O. J. Kleppa, *J. Inorg. Nucl. Chem.*, 1967, **29**, 2701-2714.
49. G. Burns Roger and S. Fyfe William, *Science*, 1964, **144**, 1001-1003.
50. R. A. Maier, A. C. Johnston-Peck and M. P. Donohue, *Adv. Funct. Mater.*, 2016, **26**, 8325-8333.
51. R. A. Serway, W. Berlinger, K. A. Müller and R. W. Collins, *Phys. Rev. B*, 1977, **16**, 4761-4768.
52. D. V. Azamat, A. G. Badalyan, A. Dejneka, V. A. Trepakov, L. Jastrabik and Z. Frait, *J. Phys. Chem. Solids*, 2012, **73**, 822-826.
53. C. M. Julien, M. Massot and C. Poinsignon, *Spectrochim. Acta. A*, 2004, **60**, 689-700.
54. H. D. Lutz, B. Müller and H. J. Steiner, *J. Solid State Chem.*, 1991, **90**, 54-60.
55. B. Ravel, M. Newville, *J. Synchrotron Rad.,* 2005, **12**, 537-541.

56. N. Cheng, S. Stambula, D. Wang, M. N. Banis, J. Liu, A. Riese, B. Xiao, R. Li, T.-K. Sham, L.-M. Liu, G. A. Botton and X. Sun, *Nat. Commun.*, 2016, **7**, 13638.
57. M. Muñoz, P. Argoul and F. Farges, *Am. Mineral.*, 2003, **88**, 694-700.
58. M. Muoz, F. Farges and P. Argoul, *Phys. Scr.*, 2005, T115, 221-222.
59. S. Sun, X. Zhou, B. Cong, W. Hong and G. Chen, *ACS Catal.*, 2020, **10**, 9086-9097.
60. Q. Song, J. Li, S. Wang, J. Liu, X. Liu, L. Pang, H. Li and H. Liu, *Small*, 2019, **15**, 1903395.
61. B. Hammer and J. K. Norskov, *Nature*, 1995, **376**, 238-240.
62. A. J. Medford, A. Vojvodic, J. S. Hummelshøj, J. Voss, F. Abild-Pedersen, F. Studt, T. Bligaard, A. Nilsson and J. K. Nørskov, *J. Catal.*, 2015, **328**, 36-42.
63. J. K. Nørskov, F. Abild-Pedersen, F. Studt and T. Bligaard, *P. Natl. Acad. Sci. USA,* 2011, **108**, 937.
64. S. Anantharaj, S. R. Ede, K. Karthick, S. Sam Sankar, K. Sangeetha, P. E. Karthik and S. Kundu, *Energy Environ. Sci.*, 2018, **11**, 744-771.
65. S. Anantharaj and S. Kundu, *ACS Energy Lett.*, 2019, **4**, 1260-1264.

ARTICLE

Table of Contents

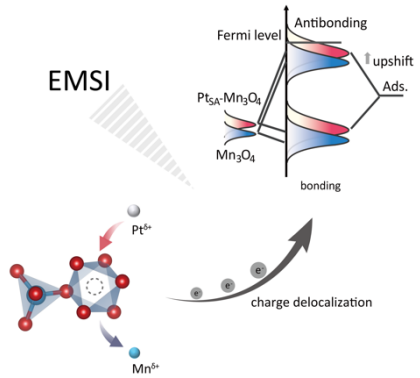

Controllable doping Pt single-atom into the octahedral sites of the spinel Mn_3O_4 lattice induced electron transfer between Pt and Mn_3O_4, which led to a moderate rise in the E_d energy level of the catalyst. Consequently, the water adsorption capacity and OH* adsorption affinity of Pt_{SA}-Mn_3O_4 were greatly enhanced and exhibited superior hydrogen evolution reaction activity.